PNAS RESEARCH ARTICLE | BIOPHYSICS AND COMPUTATIONAL BIOLOGY

Friction patterns guide actin network contraction

Alexandra Colin[a,1], Magali Orhant-Prioux[a,1], Christophe Guérin[a,1], Mariya Savinov[b,1], Wenxiang Cao[c], Benoit Vianay[d], Ilaria Scarfone[a], Aurélien Roux[e], Enrique M. De La Cruz[c], Alex Mogilner[b], Manuel Théry[a,d,2], and Laurent Blanchoin[a,d,2]

Edited by Gijsje H. Koenderink, Technische Universiteit Delft, Delft, Netherlands; received January 12, 2023; accepted August 9, 2023 by Editorial Board Member Yale E. Goldman

The shape of cells is the outcome of the balance of inner forces produced by the actomyosin network and the resistive forces produced by cell adhesion to their environment. The specific contributions of contractile, anchoring and friction forces to network deformation rate and orientation are difficult to disentangle in living cells where they influence each other. Here, we reconstituted contractile actomyosin networks in vitro to study specifically the role of the friction forces between the network and its anchoring substrate. To modulate the magnitude and spatial distribution of friction forces, we used glass or lipids surface micropatterning to control the initial shape of the network. We adapted the concentration of Nucleating Promoting Factor on each surface to induce the assembly of actin networks of similar densities and compare the deformation of the network toward the centroid of the pattern shape upon myosin-induced contraction. We found that actin network deformation was faster and more coordinated on lipid bilayers than on glass, showing the resistance of friction to network contraction. To further study the role of the spatial distribution of these friction forces, we designed heterogeneous micropatterns made of glass and lipids. The deformation upon contraction was no longer symmetric but biased toward the region of higher friction. Furthermore, we showed that the pattern of friction could robustly drive network contraction and dominate the contribution of asymmetric distributions of myosins. Therefore, we demonstrate that during contraction, both the active and resistive forces are essential to direct the actin network deformation.

cytoskeleton | contraction | friction | actin

Significance

Cell shape changes are controlled by complex sets of mechanical forces of various origins. Numerous studies have been dedicated to the role of active forces, originating from molecular motors and filament polymerization, but much less is known about the guiding role of resistive forces. Here, we show that a nonuniform distribution of friction forces between a contracting actomyosin network and its underlying substrate can direct its deformation as it contracts. Our results suggest that the contribution of resistive forces, such as viscous forces along the cell surface, can be as significant as those of active forces in driving network deformation and should be considered in mechanical models describing the regulation of cell shape and movement.

Actin and myosins are found in all eukaryotes (1–3). Myosins cross-link actin filaments, slide them along each other, and thus power large-scale network contraction (4, 5). The regulation of actomyosin contraction controls cells' shape and the mechanical forces they produce on their environment (6–8). In particular, the asymmetry of contraction directs cell deformation and orient tissue morphogenesis (9). Network deformation results from the balance between active contraction and passive resistance. The active contraction depends on the architecture of the actin network and on the amount and spatial distribution of myosins in the network (7, 10). The passive resistance is produced by network anchorages and the friction forces (11, 12). The balance of these four contributions set the rate and orientation of network deformation. Although numerous studies have focused on the mechanism that orients active contraction, the directing role of passive resistance has been much less studied. Can asymmetric friction direct a contractile network as a lagging paddle can guide a canoe?

The architecture of the actin network is defined by filament length, density, cross-linking, and their respective orientations. It can take the form of branched meshwork or bundles of filaments. Each of these modules has specific contractile properties (13). In cells, their relative dispositions form structural patterns that direct cell deformation and motion (14, 15). Structural anisotropies, such as local weakness induced by local network disassembly, generate the propagation and oscillation of contractile waves (16, 17), the maintenance of which directs the deformation and motion of poorly adhesive cells (18–20). Similarly, local structural reinforcement, by network polymerization in response to the optoactivation of Rac, for example, directs cell deformation in the opposite direction (21, 22).

The spatial distribution of myosins depends on their recruitment on actin filaments and activation by signaling pathways (23, 24). Their subcellular distributions generate patterns of contraction, asymmetric cell deformation, and migration (25–27). Reconstituted systems were used to show that spatial patterns of myosin activation determine the shape and boundaries of the contracting region of the network (10). In adherent cells, the actin retrograde flow accumulates myosins at the rear of the lamella where they form a subcellular pattern of contractile bundles propelling cells (20, 28–30) and neuronal growth cones (31). In poorly

Author contributions: A.C., M.O.-P., C.G., M.S., B.V., A.R., E.M.D.L.C., A.M., M.T., and L.B. designed research; A.C., M.O.-P., C.G., M.S., I.S., and A.M. performed research; E.M.D.L.C. contributed new reagents/analytic tools; A.C., M.O.-P., C.G., M.S., W.C., B.V., A.M., and M.T. analyzed data; and A.C., E.M.D.L.C., A.M., M.T., and L.B. wrote the paper.

The authors declare no competing interest.

This article is a PNAS Direct Submission. G.H.K. is a guest editor invited by the Editorial Board.

[1]A.C., M.O.-P., C.G., and M.S. contributed equally to this work.

[2]To whom correspondence may be addressed. Email: manuel.thery@cea.fr or laurent.blanchoin@cea.fr.

This article contains supporting information online at https://www.pnas.org/lookup/suppl/doi:10.1073/pnas.2300416120/-/DCSupplemental.

Published September 19, 2023.

adhesive cells, a global increase of cell contraction triggers a wave that concentrates myosin in the back and propels cell motion forward (32, 33). Reversal of this contraction pattern is necessary when immune cells reverse their polarity to process the antigens they encounter in the front (34). Subcellular activation patterns of myosins could also be induced with optogenetic tool to induce local contraction and asymmetric deformation contributing to cell motion (20, 35–37). At larger scales, in tissues, asymmetric localization or gradients of myosins power anisotropic tissue deformation (38–41).

The anchorages link the actin network to the extracellular matrix or to surrounding cells via integrins or cadherins (9). In the local absence of anchorages in the plasma membrane, cortical actin filaments can glide and coalesce to form contractile bundles that concentrate forces (42, 43). By contrast, filaments have limited translocation freedom in regions where anchorages are present, so they assemble thinner and pinpointed bundles (42, 44). Thus, extracellular patterns of adhesion are converted into a pattern of structure (45) and a pattern of forces (46). As a consequence, cells tend to detach from regions of lower adhesiveness and move toward regions of higher adhesiveness (47, 48). Such polarization of actomyosin network deformation can be externally induced by inducing a local detachment of the cell, which is sufficient to induce cell motion toward the opposite direction (49).

Friction forces resist the relative sliding of the actin network along its anchoring surface (50, 51) and thereby allow cell translocation (52, 53). They also limit the sliding of actin filaments along each other and thus control network deformation and rearrangements as it contracts (36, 54). In tissues, friction has been proposed to limit the instabilities and direct the self-organization of contractile waves into regular banding patterns (55). This process of directed contraction, in principle, orients network contraction toward regions of higher friction. Although the global role of friction forces has been clearly identified in the migration of poorly or nonadhesive cells (56, 57), or in the motion of encapsulated cell extracts (58), it is still unclear whether the pattern of friction can orient cell and tissue deformation. Single cells and cellular aggregates move toward less deformable regions where friction forces between the contracting actin network and the substrate are higher (59–61). At larger scales, the anisotropic pattern of friction has been proposed to account for the directed contraction of *Drosophila* apical surface during gastrulation (62), the morphogenesis of the neurectoderm in zebrafish embryos (63), and the emergence of chiral flows in the cortex of *Caenorhabditis elegans* embryos (64). However, in cells, and a fortiori in tissues, it is challenging to distinguish the effect of the friction pattern from those of structure, myosin, and adhesion patterns. These parameters influence each other and self-organize together (26, 30, 31, 65). Testing the specific role of friction pattern requires to modulate the spatial distribution of friction while all other contributions, structure, myosin, and anchorage, are homogeneous. Here, we used geometrically controlled reconstituted actomyosin networks (66), contracting either on glass or on lipid-coated surfaces (51, 67, 68), to investigate the specific role of friction in the guidance of large-scale contractions.

Results

Actin Assembly Rates Are Distinct on Glass and Lipid Micropatterns. To study the role of friction on the contraction of actomyosin networks, we used surface micropatterning to control the initial shape of the network. Our protocol to micropattern actin networks on supported lipid bilayer was inspired from several preceding methods. In brief, glass coverslips coated with a Polyethylene glycol (PEG) layer were exposed to deep Ultraviolet (UV) through a photomask in order to remove the PEG locally (69). The coverslips were then immersed in a solution containing small unilamellar vesicles (SUVs), containing 0.25% of lipids conjugated with biotin. The vesicles exploded and spread in contact with the regions presenting bare glass (70). A Nucleation Promoting Factor (NPF; Snap-Streptavidin-WA-His) was then attached to these patterned lipids via a biotin–streptavidin link. The actin polymerization mix was then added onto this micropatterned surface to generate actin networks of controlled geometries (66) (Fig. 1*A*).

We first checked that NPF was active in our conditions and could induce the assembly of a branched actin network on the micropatterned lipid bilayer (Fig. 1*B* and Movie S1), as previously shown on infinite bilayers (71, 72). We also confirmed that lipids and NPF could diffuse freely at normal rates (73, 74) before and after actin polymerization despite the immobility of the dense actin mesh (Fig. 1*C*, *SI Appendix*, Fig. S1, and Movie S2). Interestingly, we observed that the efficiency to generate an actin assembly with NPF grafted onto a lipid micropattern was an order of magnitude higher (10 times faster) than that of NPF grafted onto a glass micropattern (Fig. 1 *D* and *E* and Movie S3). Considering that network density limits network contraction (72, 75), we determined the concentrations of NPF that induced similar actin network assembly on the glass and lipid micropattern (Fig. 1 *D* and *E* and Movie S3) to investigate specifically the role of substrate friction on network contraction. Hence, in the following experiments, the concentration of NPF will be 1 μM on glass and 1 nM on lipids.

Friction Slows Down Network Deformation upon Contraction. In the following experiments, friction could arise from either 1) attachment between the actin network and the NPF or 2) nonspecific interactions between actin filaments and the surface. We rule out the first possibility for the following reasons: We monitored the initial events of branch formation and quantified that filament diffusion was the same before and after branch formation (*SI Appendix*, Fig. S2 *A* and *B*), demonstrating that the NPF does not remain attached to the actin network, confirming existing results in the literature (76). We investigated next the possibility that friction is due to the nonspecific interaction between actin filaments and the surface (glass or lipids). Therefore, we followed the diffusive movement of individual actin filaments on NPF micropatterns on a lipid or glass surface. We tracked using TIRF (total internal reflection fluorescence) microscopy the center of mass of these filaments and evaluated their translational diffusion coefficient from the Mean Square Displacement (MSD) analysis. We measured that the diffusion coefficient on glass patterns is slower than on lipid patterns, demonstrating that individual actin filaments experience greater friction when they come into contact with a glass surface than with a lipid surface (*SI Appendix*, Fig. S2 *D–F*). Moreover, when an additional blocking step with Bovine serum albumin (BSA) is performed on the NPF-coated glass surface, we found that the diffusion coefficient of actin filaments becomes similar to that of the lipid surface. This demonstrates that the contribution of NPF–actin interaction to the friction is limited (*SI Appendix*). We also tracked branches at the early stages of their formation and measured their diffusion coefficient from the MSD. Similarly, we found that branches diffuse slower on glass than on lipid micropattern, showing that they experience a higher friction (*SI Appendix*, Fig. S2 *C* and *F*). Einstein relation then allows us to conclude that the actin–glass friction is roughly three-fold greater than the actin–lipid friction (*SI Appendix*).

We then assessed the impact of the friction between the actin filaments and the underlying substrate during the actomyosin network contraction. Addition of a double-headed [heavy-meromyosin

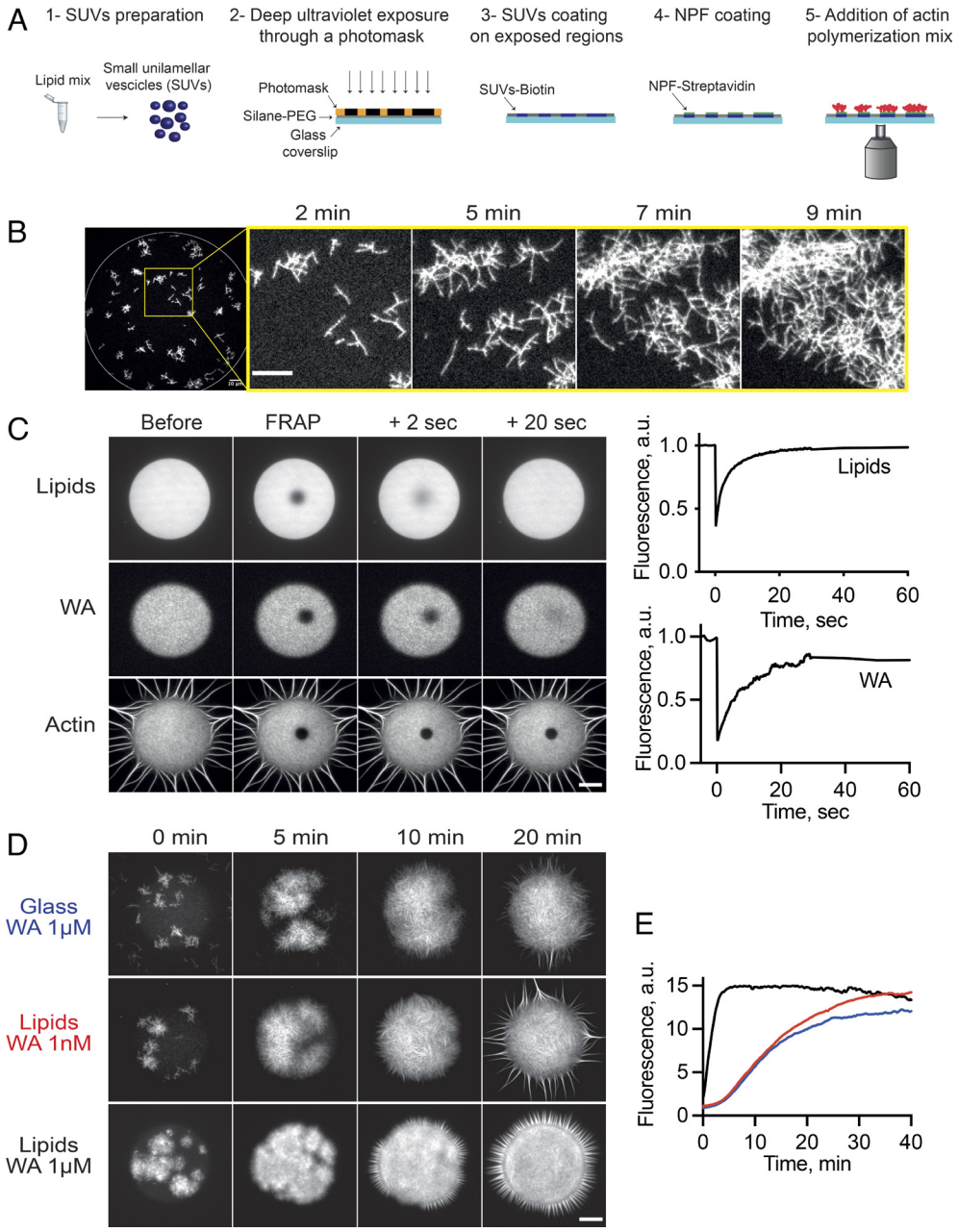

Fig. 1. Actin assembly on glass or lipid micropatterns. (*A*) Cartoon of the method to constrain branched actin network assembly on glass or lipid micropatterns. (*B*) TIRF imaging of branched actin assembly on lipid micropattern (disk, diameter 135 μm). Biochemical conditions: WA 1 nM, Actin 1 μM, Human Profilin 3 μM, Arp2/3 complex 25 nM. (Scale bar: 10 μm.) (*C*) Characterization of the diffusion property of the lipid micropattern. *Left*: TIRF imaging before and after FRAP (zone diameter: 10 μm) on lipids, NPF (WA), and Actin (after network polymerization). Biochemical conditions: disk micropattern (diameter 68 μm), WA 1 nM, Actin 1 μM, Human Profilin 3 μM, and Arp2/3 complex 25 nM. (The scale bar is 20 μm.) *Right*: Fluorescence measurements from the images on the left demonstrate that the lipids and the NPF diffuse freely in our experimental conditions. (*D*) Comparison of the efficiency of actin network growth on lipid versus glass micropatterns. TIRF imaging of branched actin assembly on lipid and glass disk micropatterns (diameter 68 μm). Biochemical conditions: NPF concentration is indicated on the figure. Actin 1 μM, Human Profilin 3 μM, and Arp2/3 complex 25 nM. (The scale bar is 20 μm.) (*E*) Kinetics of actin assembly on lipid versus glass micropattern.

(HMM)-like] myosin VI (13, 75) to a disk- or a square-shaped network on glass or lipid induced its contraction toward the center of the initial shape (Fig. 2 *A* and *B* and Movies S4 and S5).

The contraction process followed three phases (described in ref. 13) and illustrated by the variation of the area covered by the actin network over time (Fig. 2). An a) initial growth phase corresponding to the assembly of actin filaments in the first 10 min after the addition of actin monomer to the reaction mixture; b) a lag, corresponding to the loading of myosins on the actin filaments (*SI Appendix*, Fig. S4 *A*–*C*) and their local reorganization without any global deformation of the entire network; and c) the deformation by contraction of the network toward the center of the micropattern (Fig. 2 *C* and *D*). The initial delay of assembly was identical for lipid (red curve) or glass (blue curve) on disks and squares (Fig. 2 *C* and *D*). However, the lag and deformation phases were different on glass and lipids. The lag phase was shorter, and the deformation rate was faster on lipids than on glass (Fig. 2 *E* and *F*). Similar observations were made for the contraction of networks on rectangles of identical area (*SI Appendix*, Fig. S3). This showed that the lower friction on lipids than on glass facilitates actin network contraction by myosins. In addition, we also looked

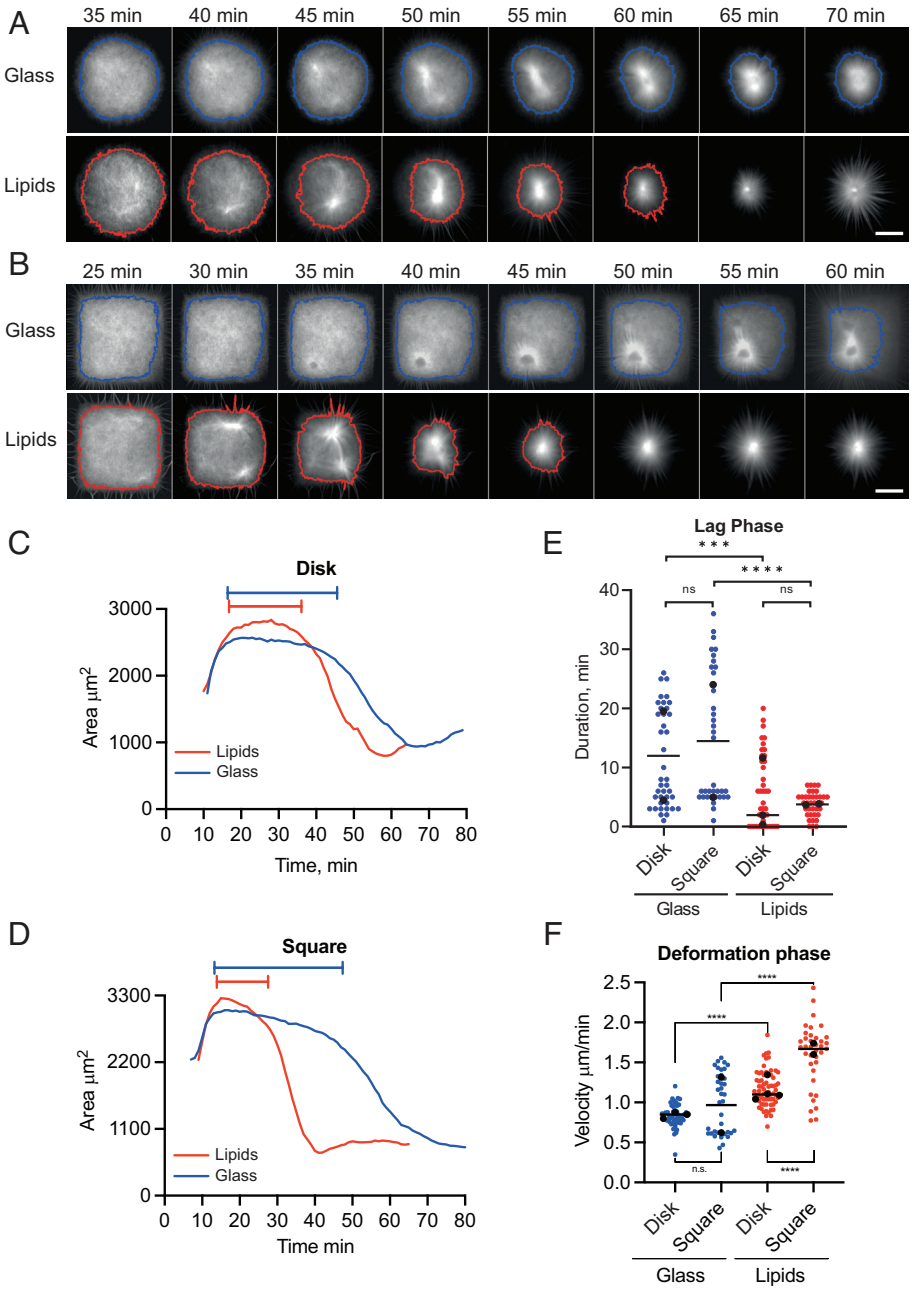

Fig. 2. NPF attachment conditions control actin network contractile response. (*A*) Kinetics of contraction of a disk-shaped actin network on glass or lipid micropattern. Time-lapse imaging of actin network contraction on a glass or lipid disk (diameter 68 µm) micropattern. The line (blue for glass; red for lipids) corresponds to the contours of the actin network (*Materials and Methods*). Biochemical conditions: On glass micropattern, WA = 1 µM; on lipid micropattern: WA = 1 nM. Actin 1 µM, Human Profilin 3 µM, Arp2/3 complex 25 nM, and Myosin VI 14 nM. (The scale bar is 20 µm.) (*B*) Kinetics of contraction of a square-shaped actin network on glass or lipid micropattern. Time-lapse imaging of actin network contraction on a glass or lipid square (length 60 µm) micropattern. The line (blue for glass; red for lipids) corresponds to the contours of the actin network (*Materials and Methods*). Biochemical conditions: On glass micropattern, WA = 1 µM; on lipid micropattern: WA = 1 nM. Actin 1 µM, Human Profilin 3 µM, Arp2/3 complex 25 nM, and Myosin VI 14 nM. (The scale bar is 20 µm.) (*C* and *D*) Measured actin area as a function of time for the lipid (red) or glass (red) conditions on disk (*C*) or square (*D*) micropattern. The period defined at the top of the graph determines the lag phase for each condition. (*E*) Duration of the lag phase preceding the contraction for the lipid or glass conditions on disk or square micropattern. Data are represented with a superplot. Disk glass: n = 40; N = 2; *median* = 7.5. Disk lipids n = 41; N = 3; *median* = 4.0. Square glass n = 37; N = 2; *median* = 7.0. Square lipids n = 37; N = 2; *median* = 4.0. Mann–Whitney statistics: disk glass/disk lipids *P* value = 0.0010***, square glass/square lipids *P* value ≤ 0.0001****, disk glass/square glass *P* value = 0.1247 ns, and disk lipids/square lipids *P* value = 0.5360 ns. (*F*) Velocity of the phase contraction phase for the lipid or glass conditions on disk or square micropattern. Data are represented with a superplot. Disk glass n = 53; N = 3; *median* = 0.8346, disk lipids n = 68; N = 4; *median* = 1.133, square glass n = 37; N=2; *median* = 1.013, and square lipids n = 37; N = 2; *median* = 1.694. Mann–Whitney statistics: disk glass/disk lipids *P* value ≤ 0.0001****, square glass/square lipids *P* value ≤ 0.0001****, disk glass/square glass *P* value = 0.2761 ns, and disk lipids/square lipids *P* value ≤ 0.0001****.

at the myosin signal at the beginning of the contraction and correlated it with the contraction velocity (*SI Appendix*, Fig. S4 *D–F*). Assuming that the contractile force is proportional to the myosin concentration and the velocity is equal to the ratio of the force and the friction coefficient, the slope of the myosin concentration–velocity relation is inversely proportional to the friction coefficient. Thus, the ratio of the slopes for glass and lipid conditions gives the ratio between the two respective frictions. The data reported in *SI Appendix*, Fig. S4*F* indeed show that a slower velocity is generated on glass, compared to that on lipid, for the same myosin concentration, and gives the ratio of 3 between the respective slopes, confirming the independent

friction estimates made by measuring diffusion and using Einstein relation (*SI Appendix*, Fig. S2).

Friction Limits Large-Scale Coordination of Network Contraction. During this study, we noticed that network deformation seemed more uniform and coordinated on lipids than on glass. To characterize this, we photobleached a grid in the network and monitored its deformation during the contraction process. We found that on glass, local regions could initiate their deformation independently, while on lipids, the deformed regions formed a continuum and contracted together across the network (Fig. 3*A* and *SI Appendix*, Fig. S5). To further quantify this, we tracked actin network deformation by particle image velocimetry (Fig. 3 *B* and *C*). For the analysis, we decomposed the square in four quadrants and summed the velocities of the moving parts in each quadrant. Measurements showed that the deformation of the four quadrants was not similar nor synchronized on glass, but they were precisely coordinated on lipids (Fig. 3 *B* and *C* and *SI Appendix*, Fig. S6). Interestingly, this difference of spatial and temporal coordination during contraction had an impact on the position of the point of convergence of the contraction process, which was closest to the center of the initial shape on lipids than on glass (Fig. 3*D* and Movies S6 and S7). This showed that the lower friction on lipids than on glass allowed a more integrated and coordinated actomyosin contraction.

A Pattern of Friction Can Guide Network Contraction. The abovementioned effect of friction on the rate and coordination of the contraction process suggested that heterogeneity in the friction coefficient between the actin network and the underlying substrate might direct network contraction. To test this hypothesis, we developed a method to generate a heterogeneous friction pattern below uniform and geometrically controlled actin networks (*SI Appendix*, Fig. S7*A*). We used a digital micromirror device (DMD) to photoactivate distinct regions sequentially and coat them with distinct components (*Materials and Methods* and *SI Appendix*, Fig. S7*A*). On a PEG layer, we generated disks, squares, or rectangles, half of which was made of bare glass coated with 1 μM NPF, and the other half was coated with lipids and 1 nM NPF to obtain similar actin polymerization kinetics on the two halves and thus a homogeneous network over the entire micropattern. We confirmed that lipids and WA diffused on the lipid half and not on the glass half (*SI Appendix*, Fig. S7*B*) and that the networks contracted according to the three phases described previously (*SI Appendix*, Fig. S8).

Strikingly, while networks on homogeneous disk-shape lipid micropatterns contracted precisely toward the centroid of the initial geometry, they showed a clear off-centering toward the region of higher friction on heterogeneous glass–lipid micropatterns (Fig. 4 *A* and *B* and Movies S9–S14). This deviation resulted from the faster deformation of the actomyosin network on lipids than on glass (*SI Appendix*, Fig. S8). We tested additional patterns of friction in squares and rectangles and noticed that the network compacts to a point which is biased toward the center of the higher friction region (Fig. 4 *C*–*F*). These results demonstrated that a friction pattern can guide actomyosin network deformation.

Numerical Simulations Account for the Trajectories of Myosin Spots during Network Contraction. To further understand the way actomyosin networks deform as they contract, we turned to computational modeling. We model the actomyosin network as a two-dimensional viscoelastic network with active contractile stresses generated by myosin concentrated in several foci (77). The internal (passive viscoelastic and active contractile) stresses in the network are balanced by friction between the network and substrate (glass or lipid), which we model as effective viscous drag with the drag on glass higher than that on lipid. This model is implemented as a network of nodes connected by a viscous dashpot with the substrate. Neighboring nodes are connected by the viscous dashpot and elastic (nonlinear) spring in series responsible for viscous and elastic deformations inside the network (*SI Appendix*, *Model Description* and Fig. 5*A*).

We first simulated the contraction of the network on homogeneous lipid square, with initial myosin foci appearing in four corners of the square (Fig. 5*B* and Movie S16). The simulations showed the temporal sequence of the network deformation like those observed experimentally (Fig. 2*B*). Specifically, the simulations correctly predict that the network corners get rounded right after the onset of the contraction (Fig. 5*B*). Note also that the area near the center of the network did not deform until late stage of contraction (Fig. 5*B*), which is also observed in experiments (Fig. 3*A*). We then plotted the predicted myosin foci's trajectories for homogeneous patterns. Interestingly, for the homogeneous pattern, the model predicts that regardless of the initial positions and even number of myosin spots, the spots drifted straight to the center of the square and converged to it (Fig. 5*C*). Importantly, the model predicted that to generate the observed ratio of the contractile rates on glass and lipid, the respective ratio of the friction coefficients has to be approximately 3 (*SI Appendix*), as is already established by two independent experimental estimates.

Remarkably, when a heterogeneous pattern of friction was simulated with the exact same initial myosin distribution, the final point of contraction was shifted toward the side of high friction as observed on the experimental data (Fig. 5*D* and Movie S17). Furthermore, for the square homogeneous or heterogeneous patterns, we found that regardless of the initial position and number of myosin foci, the foci drifted straight to the center of the friction pattern and then converged to it (Fig. 5 *C* and *D* and see *SI Appendix*, Fig. S9 *A* and *B* for examples with different positions of myosin foci). This is reminiscent of the ballistic contractility previously described (77). Finally, the trajectories predicted on homogeneous or heterogeneous rectangles showed myosin foci first converging to the point of intersection of the bisecting lines of the angles and then moving to their destination, defined by the distinct weights of the two friction patterns. (*SI Appendix*, Fig. S9 *C*–*F*).

Two contraction features are illustrated by these trajectories. First, the global character of the contraction: myosin foci integrate large areas in the definition of their motion, which is largely the consequence of the highly interconnected character of the actomyosin network and global propagation of the internal stresses (*SI Appendix*, *Model Description*). Second, the predicted locations of the convergence points of the contracted heterogeneous pattern are largely insensitive to the initial myosin distributions (and to the number of myosin foci) but determined by the adhesion distribution.

Consequently, heterogeneity of contractility (initial myosin distribution) does not explain nor impact contraction asymmetry. Although the contraction is local and randomly initialized by myosin foci, a combination of network geometry and external friction heterogeneity leads to a robust global polarized contraction. Thus, our model proposes that the friction pattern can dominate over the initial distribution of contractility to drive contraction asymmetry.

Friction Acts as a Master Control of Symmetry of Actomyosin Meshwork Contraction. We tested the predictions of the model by analyzing the localization and trajectories of myosin foci in our experimental data. Foci formed rapidly and were randomly

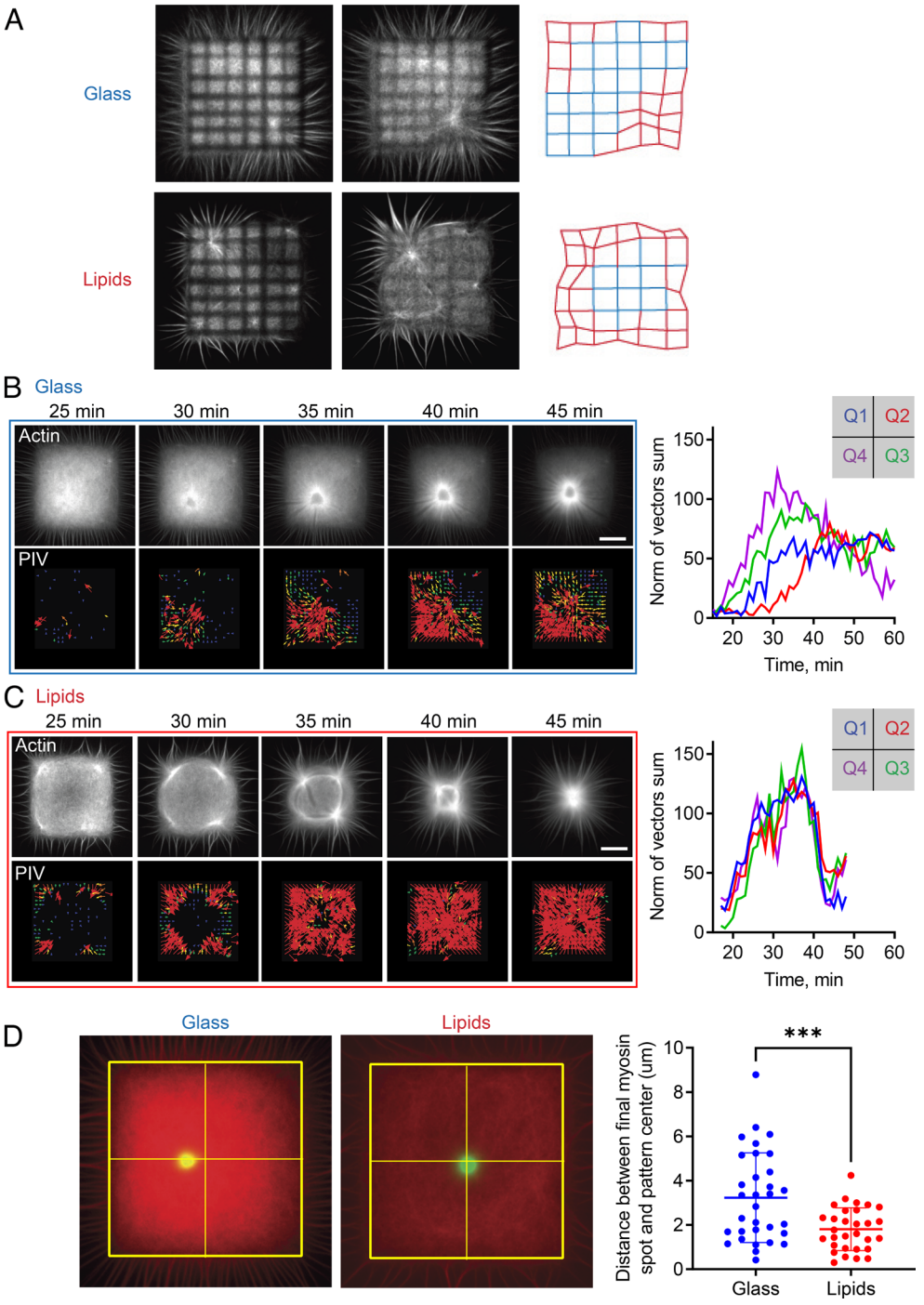

Fig. 3. Lower friction improves the coordination of the contraction process. (*A*) Local deformation of the actin network. A photobleached grid shape was performed on actin networks polymerized on glass or lipid micropatterns. Then, deformations of the actin network were followed by following the grid deformation. (*B*) *Left Top*: Example of an actin network grown on glass substrate pattern used for PIV analysis. *Left Bottom*: PIV analysis of the actin network shown above. *Right*: Resultant of vector sum for each quadrant defined on the pattern as a function of time (*Materials and Methods*). (*C*) Same as *B* with an actin network grown on lipid substrate. (*D*) *Left*: Snapshots of the final position of myosin spot for actin networks grown on glass or lipid square micropattern. *Right*: Quantification of the distance between the final myosin spot and the pattern center for networks grown on glass or lipids. N = 2 independent replicates with n = 18 and n = 12 patterns for the lipids condition and n = 19 and n = 13 patterns for the glass condition. Individual points for each pattern are represented. Mean and SD are plotted on top of the points. Unpaired *t* test: *P* value ≤ 0.001***. Biochemical conditions for Fig. 3: On glass micropattern, WA = 1 μM; on lipid micropattern: WA = 1 nM. Actin 1 μM, Human Profilin 3 μM, Arp2/3 complex 25 nM, and Myosin VI 14 nM.

distributed in networks assembled on homogeneous square lipid micropatterns (Fig. 6*A*). The heterogeneity of these initial distributions, which could be quite asymmetric, and sometimes even made of a single and off-centered focus, did not impact the position of the convergence point, at the square center, nor the trajectories, which were directed straight toward it (Fig. 6*A* and Movie S10). These observations were consistent with the model (Fig. 5 *B* and *C*) and demonstrate that the actomyosin network contraction integrates the entire shape of the network independently of the asymmetry of myosins distribution.

Tracking myosin foci on homogeneous rectangular lipid micropatterns confirmed the above conclusions on the absence of

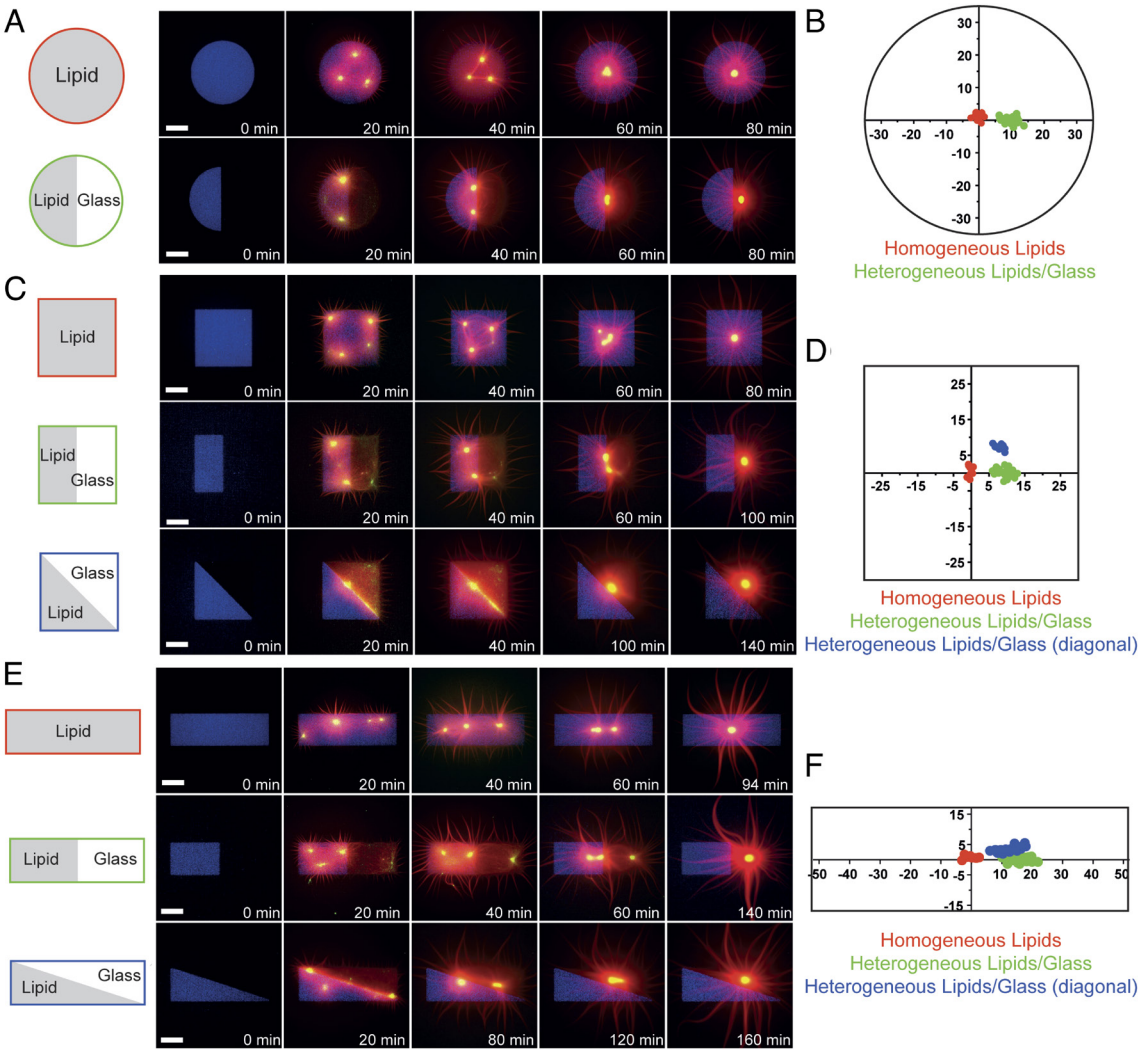

Fig. 4. Friction pattern directs network contraction. Time-lapse imaging of actin network contraction on full lipid or heterogeneous disks (*A*), full lipid or heterogeneous squares (*C*), and full lipid or heterogeneous rectangles (*E*). Biochemical conditions: Actin 1 μM, Human Profilin 3 μM, Arp2/3 complex 25 nM, and Myosin VI 10 nM. Pattern dimensions: disks 64 μm diameter; squares 60 μm length; rectangles 104 μm × 34 μm. The pattern is represented in blue, actin in red, and myosin in green. (Scale bar: 20 μm.) (*B*, *D*, and *F*) Plot of the myosin dots coordinates at the end of contraction for the different shapes. All coordinates were measured and compared to the centroid (x = 0, y = 0) of the whole pattern. Red dots correspond to the coordinates of the full pattern made of lipid, green dots correspond to the coordinates of the symmetrical heterogeneous pattern and the blue dots correspond to the coordinates of the asymmetrical heterogeneous patterns. Disk full lipids: N = 3, n = 11 patterns. Heterogeneous disk: N = 4, n = 26 patterns. Square full lipids: N = 2, n = 9 patterns. Heterogeneous square: N = 4, n = 29 patterns. Asymmetrical heterogeneous square: N = 2, n = 11 patterns. Rectangle full lipids: N = 2, n = 8 patterns. Heterogeneous rectangle: N = 4, n = 24 patterns. Asymmetrical heterogeneous rectangle: N = 3, n = 21 patterns.

impact of the asymmetry of myosin distribution. They also showed that myosin foci first moved along angle bisecting lines and then reorient toward the rectangle center. These observations were also consistent with the model (Fig. 5 *C* and *E* and *SI Appendix*, Fig. S9 *E* and *F*) and further demonstrated that the contraction process integrate local and global network geometry, as previously shown (10), regardless of the initial pattern of myosins.

Importantly, during the contraction of actin networks assembled on heterogeneous square patterns of glass and lipids, we also found that myosin foci could be observed above both types of substrates (Fig. 6*C* and Movies S11 and S12). This confirmed that network density and architectures were similar on glass and on lipids and that the initial localization of myosin foci was not determined by the strength of the underlying friction. The trajectories were initially not all directed toward network final convergence point, likely due to the asynchrony of the contraction described earlier (Fig. 2) but then all move toward the off-centered destination regardless of their position above glass or lipids, further confirming that the network integrated the entire geometry and the entire heterogeneity of the underlying friction pattern (Fig. 6*C*). Foci trajectories during the contraction of actin networks assembled on heterogeneous rectangular patterns of glass and lipids confirmed these two conclusions on the dominant roles of network geometry and friction pattern over the initial distribution of myosins (Fig. 6*D*).

Discussion

Actin network architecture, myosin distribution, and network anchorages are intimately related. They coassemble and influence each other in complex feedback loops. Indeed, adhesion primes filament assembly (78, 79), dense filament areas recruit more myosins (80, 81) and contractile forces promote the enlargement of adhesions (82, 83). It is therefore difficult to attribute the deformation process of the contracting network to one or the other parameter. Most of previous works were focused on the steering

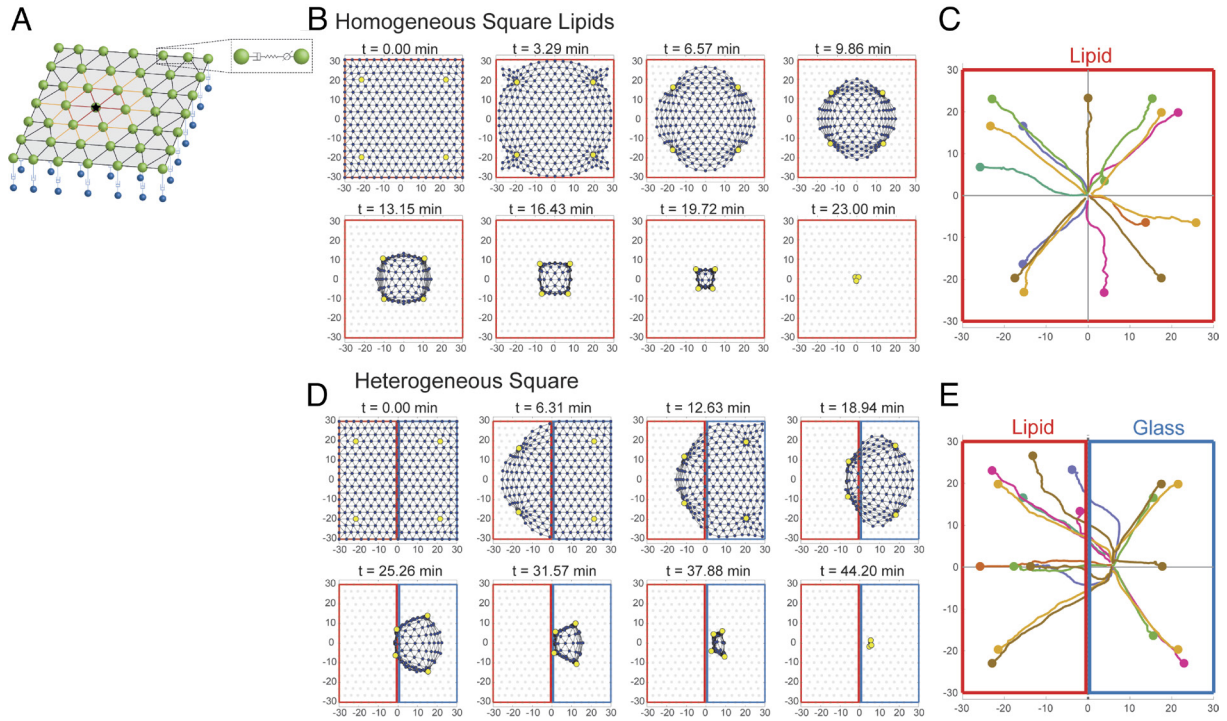

Fig. 5. The computational model recapitulates the contraction kinetics and predicts the trajectories of myosin spots during the network contraction. (*A*) Scheme of the computational model describing the network as a viscoelastic network of nodes and links. Each node is connected by a dashpot with the substrate. The dashpot is responsible for the friction (higher on glass, lower on lipid). Neighboring nodes are connected by dashpot/spring in series responsible for viscous and elastic deformations inside the network. In addition, links connecting pairs of nodes, one of which is occupied by a myosin dot (shown by a star), are contractile. (*B*) Sequence of deformations predicted by the model for an actin network polymerized on a homogeneous square lipid micropattern and contracted by myosin dots (yellow nodes). (*C*) Prediction of myosin trajectories for an actin network contracting on a homogeneous square lipid micropattern. (*D*) Sequence of deformations predicted by the model for an actin network polymerized on a heterogeneous square micropattern and contracted by myosin dots (yellow nodes). (*E*) Prediction of myosin trajectories for an actin network contracting on a heterogeneous square micropattern.

role of motors distribution since it powers the contraction process (84, 85). In vitro experiments revealed the role of network architecture in modulating the rate of network deformation by its impact on the connectivity of the contractile network (13, 72, 75).

Our study uses micropatterns on two different substrates (glass and lipids) which exhibit different frictions to precisely control the initial geometry and density of the actin network. This enabled us to study the symmetry of contraction in these conditions with respect to the initial actin network geometry. We have shown that contraction ends at the centroid of the pattern with uniform friction. We have also shown that friction is a key player in controlling contraction velocity (Figs. 2 and 3) where previous work studied the role of network cross-linking to the surface on its contraction (67, 86, 87).

By developing a method to create heterogeneous micropatterns with different boundary between regions of different friction, we have demonstrated that the pattern of friction drives the contraction asymmetry and more importantly that the friction pattern dominates the contribution of asymmetric distribution of myosins on the patterns (Fig. 6).

Here, we clearly establish the key role of friction pattern in the guidance of network deformation during contraction. This implies for cells and tissues that homogeneous contractile networks, made of even distribution of actin filament and myosins, can contract asymmetrically if their anchorages are not evenly distributed, or if the interaction between the network and its underlying substrate is not identical all over the network.

Our numerical simulations of a viscoelastic contractile network and our experimental data also show the less intuitive result that the friction pattern can guide network contraction in a quite robust manner that dominates the contribution of a heterogeneous distribution of myosins. In physiological conditions, this implies that morphogenetic processes can result from the local recruitment and activation of myosins by signaling but that the role of nonspecific adhesion is also key in the establishment of the final orientation of the deformation process. Thus, both orientations of the powering force and the resistive forces are essentials, as well known by sailors which efficiently combine the use of wind orientation in the sails to propel the boat and the rudder blade orientation to establish its final direction.

Materials and Methods

Protein Expression, Purification, and Labeling. Actin was purified from rabbit skeletal-muscle acetone powder (88). Actin was labeled on lysines with Alexa 568 (89). All experiments were carried out with 5% labeled actin. The Arp2/3 complex was purified from the calf thymus according to ref. 90. Human profilin was expressed in BL21 DE3 pLys *Escherichia coli* cells and purified according to ref. 91. Double-headed porcine myosin VI with bound calmodulin was purified from Sf9 cells by FLAG affinity chromatography (92, 93). Human WASp-WA (Snap-Streptavidin-WA-His) (pET plasmid) was expressed in Rosettas 2 (DE3) pLysS (Merck, 71403) and purified according to ref. 94.

Lipid Micropatterning. Deep UV exposure through a chrome-photomask for 45 s creates micropatterns on Silane-PEG coverslip (*SI Appendix*). The coverslip is then mounted in a 70-μm height flow chamber (with a Silane-PEG slide on top, double-sided tape, Lima ref 1820080). Thirty microliters of SUV lipid solution (*SI Appendix*) is then immediately perfused in the flow chamber. After 10 min of incubation at room temperature, the flow chamber is rinsed with 1 mL of SUV buffer. The diffusivity of the lipid bilayer was checked before each

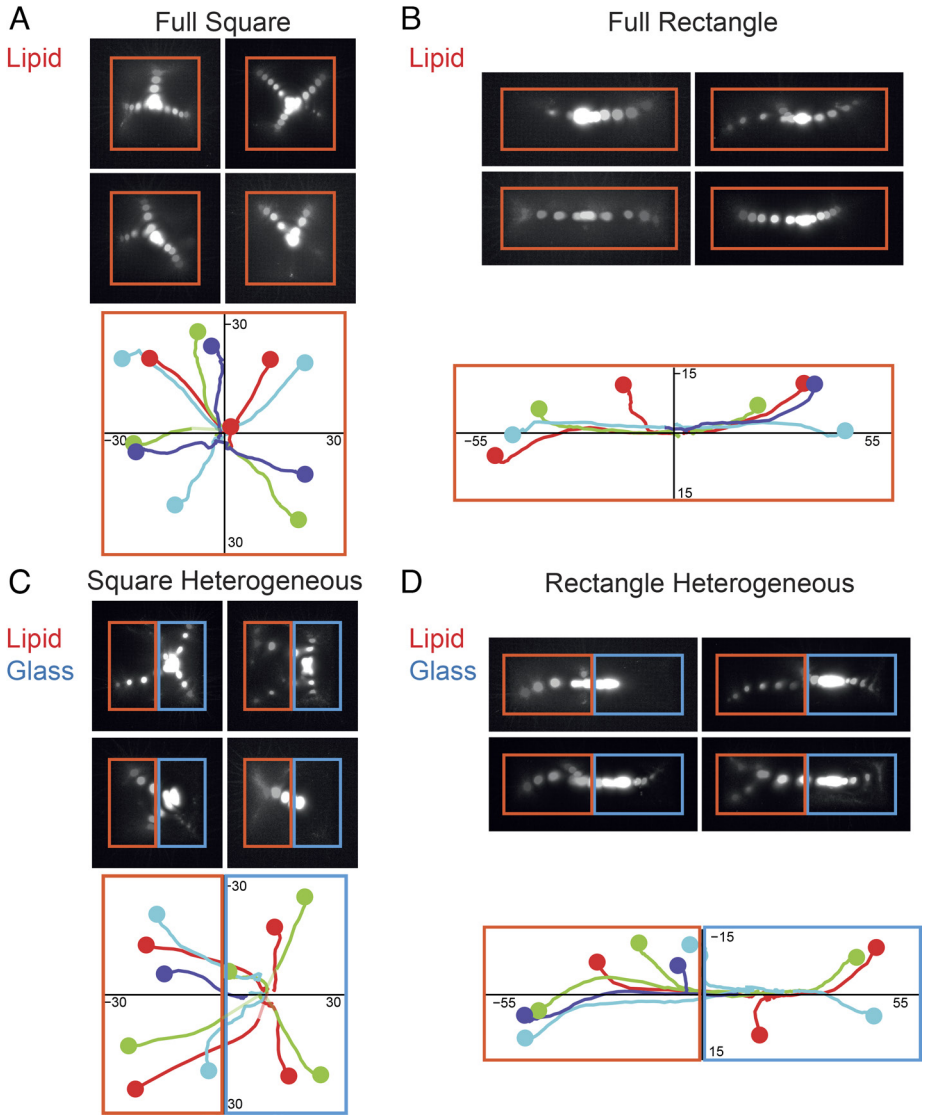

Fig. 6. Friction pattern robustly drives network contraction despite uneven distribution of myosin. *Top*: Four examples of temporal projections of myosin detection on a full-square micropattern (*A*), a full-rectangle micropattern (*B*), a heterogeneous square micropattern (*C*), and a heterogeneous rectangle micropattern (*D*). *Bottom*: Detection of myosin spots as a function of time (see *Materials and Methods* for details). Each example of the above images is represented with a single color. The initial time of the trajectory is represented with a bigger dot.

experiment with Fluorescence Recovery After Photobleaching (FRAP) analysis of the lipid bilayer.

Patterning for Heterogeneity Experiments. Full, symmetrical and asymmetrical patterns were generated on a Nikon eclipse inverted microscope equipped with the Primo Digital Micromirror Device (DMD) (Alveole) (95).

Actin Polymerization and Contraction. Actin polymerization and contraction were induced by injection in the flow chamber of a reaction mixture containing 1 μM actin monomers (12% labeled with Alexa 568), 3 μM profilin, 25 nM Arp2/3 complex, and 14 nM of HMM-myosin VI (GFP labeled). This protein mixture was diluted in freshly prepared buffer containing 10 mM Hepes (pH 7.5), 3 mM ATP, 27 mM DTT, 1 mM EGTA, 50 mM KCl, 5 mM $MgCl_2$, 3 mg/mL glucose, 20 μg/mL catalase, 100 μg/mL glucose oxidase, and 0.25% w/v methylcellulose. The sample was then closed with VALAP to avoid evaporation.

Imaging. Time courses of actin assembly and contraction on homogeneous patterns were acquired on a TIRF microscope (Roper Scientific) equipped with an iLasPulsed system and an Evolve camera (EMCCD 512 × 512, pixel = 16 μm) using a 60× 1.49 objective lens. Microscope and devices were driven by MetaMorph software (Molecular Devices). For heterogeneous patterns, image acquisition was done on a Nikon Eclipse Ti2 inverted microscope equipped with an S Plan fluor ELWD 40×/0,60 objective and a Hamamatsu ORCA Flash 4.0 LT camera. The microscope and equipment were driven by MicroManager software.

Image Analysis. Image analysis was performed using Fiji (96), RStudio, and GraphPad Prism.

Statistical Analysis. We used Mann–Whitney tests (nonparametric test) performed in GraphPad Prism software.

Computational Modeling. We model the actomyosin network as a contractile viscoelastic medium represented by a lattice of actin and myosin nodes connected to each other by spring-like links and to the substrate by adhesive dashpots. The network's deformations are simulated numerically by solving force balance equations. Details of the model and numerical solutions are in *SI Appendix*.

Data, Materials, and Software Availability. All study data are included in the article and/or supporting information.

ACKNOWLEDGMENTS. We thank C. Copos for help with modeling. This work was supported by the European Research Council [Consolidator Grant 771599 (ICEBERG) awarded to M.T. and Advanced Grant 741773 (Adaptive Actin

Architectures) awarded to L.B.]. This work was also supported by the MuLife imaging facility, which is funded by Grenoble Alliance for Integrated Structural, a program from the Chemistry Biology Health Graduate School of University Grenoble Alpes (ANR-17-EURE-0003). M.S. and A.M. were supported by NSF grant DMS 1953430 and 2052515 awarded to A.M. E.M.D.L.C. and W.C. were supported by the NIH through award R35-GM136656 awarded to E.M.D.L.C.

Author affiliations: [a]Université Grenoble-Alpes, CEA, CNRS, UMR5168, Interdisciplinary Research Institute of Grenoble, CytoMorpho Lab, Grenoble 38054, France; [b]Courant Institute of Mathematical Sciences, New York University, New York, NY 10012; [c]Department of Molecular Biophysics and Biochemistry, Yale University, New Haven, CT 06520-8114; [d]University of Paris, INSERM, Commissariat à l'énergie atomique et aux énergies alternatives, UMRS1160, Institut de Recherche Saint Louis, CytoMorpho Lab, Hôpital Saint Louis, Paris 75010, France; and [e]Department of Biochemistry, University of Geneva, CH-1211 Geneva, Switzerland

1. M. Kollmar, S. Mühlhausen, Myosin repertoire expansion coincides with eukaryotic diversification in the Mesoproterozoic era. *BMC Evol. Biol.* **17**, 211 (2017).
2. M. A. Hartman, J. A. Spudich, The myosin superfamily at a glance. *J. Cell Sci.* **125**, 1627–1632 (2012).
3. B. Wickstead, K. Gull, The evolution of the cytoskeleton. *J. Cell Biol.* **194**, 513–525 (2011).
4. J. R. Sellers, Myosins: A diverse superfamily. *Biochim. Biophys. Acta–Mol. Cell Res.* **1499**, 3–22 (2000).
5. J. Robert-Paganin, O. Pylypenko, C. Kikuti, H. L. Sweeney, A. Houdusse, Force generation by myosin motors: A structural perspective. *Chem. Rev.* **120**, 5–35 (2020).
6. L. Blanchoin, R. Boujemaa-Paterski, C. Sykes, J. Plastino, Actin dynamics, architecture, and mechanics in cell motility. *Physiol. Rev.* **94**, 235–263 (2014).
7. M. Murrell, P. W. Oakes, M. Lenz, M. L. Gardel, Forcing cells into shape: The mechanics of actomyosin contractility. *Nat. Rev. Mol. Cell Biol.* **16**, 486–498 (2015).
8. C.-P.P. Heisenberg, Y. Bellaïche, Forces in tissue morphogenesis and patterning. *Cell* **153**, 948–962 (2013).
9. D. N. Clarke, A. C. Martin, Actin-based force generation and cell adhesion in tissue morphogenesis. *Curr. Biol.* **31**, R667–R680 (2021).
10. M. Schuppler, F. C. Keber, M. Kröger, A. R. Bausch, Boundaries steer the contraction of active gels. *Nat. Commun.* **7**, 13120 (2016).
11. L. Kurzawa *et al.*, Dissipation of contractile forces: The missing piece in cell mechanics. *Mol. Biol. Cell* **28**, 1825–1832 (2017).
12. L. B. Case, C. M. Waterman, Integration of actin dynamics and cell adhesion by a three-dimensional, mechanosensitive molecular clutch. *Nat. Cell Biol.* **17**, 955–963 (2015).
13. A.-C. Reymann *et al.*, Actin network architecture can determine myosin motor activity. *Science* **336**, 1310–1314 (2012).
14. K. M. Yamada, M. Sixt, Mechanisms of 3D cell migration. *Nat. Rev. Mol. Cell Biol.* **20**, 738–752 (2019).
15. M. Schaks, G. Giannone, K. Rottner, Actin dynamics in cell migration. *Essays Biochem.* **63**, 483–495 (2019).
16. M. Bornens, M. Paintrand, C. Celati, The cortical microfilament system of lymphoblasts displays a periodic oscillatory activity in the absence of microtubules: Implications for cell polarity. *J. Cell Biol.* **109**, 1071–1083 (1989).
17. E. Paluch, M. Piel, J. Prost, M. Bornens, C. Sykes, Cortical actomyosin breakage triggers shape oscillations in cells and cell fragments. *Biophys. J.* **89**, 724–733 (2005).
18. W. Shih, S. Yamada, Myosin IIA dependent retrograde flow drives 3D cell migration. *Biophys. J.* **98**, L29–L31 (2010).
19. P. Maiuri *et al.*, Actin flows mediate a universal coupling between cell speed and cell persistence. *Cell* **161**, 374–386 (2015).
20. P. R. O'Neill *et al.*, Membrane flow drives an adhesion-independent amoeboid cell migration mode. *Dev. Cell* **46**, 9–22.e4 (2018).
21. S. de Beco *et al.*, Optogenetic dissection of Rac1 and Cdc42 gradient shaping. *Nat. Commun.* **9**, 1–13 (2018).
22. A. Mehidi *et al.*, Transient activations of Rac1 at the lamellipodium tip trigger membrane protrusion. *Curr. Biol.* **29**, 2852–2866.e5 (2019).
23. W. M. Bement *et al.*, Activator–inhibitor coupling between Rho signalling and actin assembly makes the cell cortex an excitable medium. *Nat. Cell Biol.* **17**, 1471–1483 (2015).
24. M. Graessl *et al.*, An excitable Rho GTPase signaling network generates dynamic subcellular contraction patterns. *J. Cell Biol.* **216**, 4271–4285 (2017).
25. E. L. Barnhart, K.-C. Lee, K. Keren, A. Mogilner, J. A. Theriot, An adhesion-dependent switch between mechanisms that determine motile cell shape. *PLoS Biol.* **9**, e1001059 (2011).
26. E. L. Barnhart, K.-C. Lee, G. M. Allen, J. A. Theriot, A. Mogilner, Balance between cell–substrate adhesion and myosin contraction determines the frequency of motility initiation in fish keratocytes. *Proc. Natl. Acad. Sci. U.S.A.* **112**, 5045–5050 (2015).
27. H. Blaser *et al.*, Migration of zebrafish primordial germ cells: A role for myosin contraction and cytoplasmic flow. *Dev. Cell* **11**, 613–627 (2006).
28. D. T. Burnette *et al.*, A role for actin arcs in the leading-edge advance of migrating cells. *Nat. Cell Biol.* **13**, 371–382 (2011).
29. J. R. Beach *et al.*, Actin dynamics and competition for myosin monomer govern the sequential amplification of myosin filaments. *Nat. Cell Biol.* **19**, 85–93 (2017).
30. L. Yolland *et al.*, Persistent and polarized global actin flow is essential for directionality during cell migration. *Nat. Cell Biol.* **21**, 1370–1381 (2019).
31. Q. Yang, X.-F. Zhang, T. D. Pollard, P. Forscher, Arp2/3 complex-dependent actin networks constrain myosin II function in driving retrograde actin flow. *J. Cell Biol.* **197**, 939–956 (2012), 10.1083/jcb.201111052.
32. V. Ruprecht *et al.*, Cortical contractility triggers a stochastic switch to fast amoeboid cell motility. *Cell* **160**, 673–685 (2015).
33. L. Barbier *et al.*, Myosin II activity is selectively needed for migration in highly confined microenvironments in mature dendritic cells. *Front. Immunol.* **10**, 1–9 (2019).
34. M. Chabaud *et al.*, Cell migration and antigen capture are antagonistic processes coupled by myosin II in dendritic cells. *Nat. Commun.* **6**, 7526 (2015).
35. L. Valon, A. Marín-Llauradó, T. Wyatt, G. Charras, X. Trepat, Optogenetic control of cellular forces and mechanotransduction. *Nat. Commun.* **8**, 14396 (2017).
36. P. W. Oakes *et al.*, Optogenetic control of RhoA reveals zyxin-mediated elasticity of stress fibres. *Nat. Commun.* **8**, 15817 (2017).
37. K. Hennig *et al.*, Stick-slip dynamics of cell adhesion triggers spontaneous symmetry breaking and directional migration of mesenchymal cells on one-dimensional lines. *Sci. Adv.* **6**, 1–13 (2020).
38. M. Rauzi, P. Verant, T. Lecuit, P.-F. Lenne, Nature and anisotropy of cortical forces orienting Drosophila tissue morphogenesis. *Nat. Cell Biol.* **10**, 1401–1410 (2008).
39. M. Rauzi, P.-F. Lenne, T. Lecuit, Planar polarized actomyosin contractile flows control epithelial junction remodelling. *Nature* **468**, 1110–1114 (2010).
40. N. L. Nerurkar, C. H. Lee, L. Mahadevan, C. J. Tabin, Molecular control of macroscopic forces drives formation of the vertebrate hindgut. *Nature* **565**, 480–484 (2019).
41. N. C. Heer *et al.*, Actomyosin-based tissue folding requires a multicellular myosin gradient. *J. Cell Sci.* **130**, 1876–1886 (2017).
42. T. Vignaud *et al.*, Stress fibres are embedded in a contractile cortical network. *Nat. Mater.* **20**, 410–420 (2021).
43. J. I. Lehtimäki, E. K. Rajakylä, S. Tojkander, P. Lappalainen, Generation of stress fibers through myosin-driven reorganization of the actin cortex. *Elife* **10**, 1–43 (2021).
44. J. Colombelli *et al.*, Mechanosensing in actin stress fibers revealed by a close correlation between force and protein localization. *J. Cell Sci.* **122**, 1665–1679 (2009).
45. M. Théry, A. Pépin, E. Dressaire, Y. Chen, M. Bornens, Cell distribution of stress fibres in response to the geometry of the adhesive environment. *Cell Motil. Cytoskeleton* **63**, 341–355 (2006).
46. K. Mandal, A. Asnacios, B. Goud, J.-B. Manneville, Mapping intracellular mechanics on micropatterned substrates. *Proc. Natl. Acad. Sci. U.S.A.* **113**, E7159–E7168 (2016).
47. T. J. Autenrieth *et al.*, Actomyosin contractility and RhoGTPases affect cell-polarity and directional migration during haptotaxis. *Integr. Biol. (Camb).* **8**, 1067–1078 (2016).
48. F. Senger *et al.*, Spatial integration of mechanical forces by α-actinin establishes actin network symmetry. *J. Cell Sci.* **132**, jcs236604 (2019).
49. A. B. Verkhovsky, T. M. Svitkina, G. G. Borisy, Self-polarization and directional motility of cytoplasm. *Curr. Biol.* **9**, 11–20 (1999).
50. Y. Aratyn-Schaus, M. L. Gardel, Transient frictional slip between integrin and the ECM in focal adhesions under myosin II tension. *Curr. Biol.* **20**, 1145–1153 (2010).
51. I. Linsmeier *et al.*, Disordered actomyosin networks are sufficient to produce cooperative and telescopic contractility. *Nat. Commun.* **7**, 12615 (2016).
52. M. F. Fournier, R. Sauser, D. Ambrosi, J.-J. Meister, A. B. Verkhovsky, Force transmission in migrating cells. *J. Cell Biol.* **188**, 287–297 (2010).
53. P. Nordenfelt, H. L. Elliott, T. A. Springer, Coordinated integrin activation by actin-dependent force during T-cell migration. *Nat. Commun.* **7**, 1–15 (2016).
54. M. P. Murrell, M. L. Gardel, Actomyosin sliding is attenuated in contractile biomimetic cortices. *Mol. Biol. Cell* **25**, 1845–1853 (2014).
55. E. Hannezo, B. Dong, P. Recho, J.-F. Joanny, S. Hayashi, Cortical instability drives periodic supracellular actin pattern formation in epithelial tubes. *Proc. Natl. Acad. Sci. U.S.A.* **112**, 201504762 (2015).
56. M. Bergert *et al.*, Force transmission during adhesion-independent migration. *Nat. Cell Biol.* **17**, 524–529 (2015).
57. A. Reversat *et al.*, Cellular locomotion using environmental topography. *Nature* **582**, 582–585 (2020).
58. R. Sakamoto, Z. Izri, Y. Shimamoto, M. Miyazaki, Y. T. Maeda, Geometric trade-off between contractile force and viscous drag determines the actomyosin-based motility of a cell-sized droplet. *Proc. Natl. Acad. Sci. U.S.A.* **119**, e2121147119 (2022).
59. C. M. Lo, H. B. Wang, M. Dembo, Y.-L. Wang, Cell movement is guided by the rigidity of the substrate. *Biophys. J.* **79**, 144–152 (2000).
60. M. L. Gardel *et al.*, Traction stress in focal adhesions correlates biphasically with actin retrograde flow speed. *J. Cell Biol.* **183**, 999–1005 (2008).
61. R. Sunyer *et al.*, Collective cell durotaxis emerges from long-range intercellular force transmission. *Science* **353**, 1157–1161 (2016).
62. S. Chanet *et al.*, Actomyosin meshwork mechanosensing enables tissue shape to orient cell force. *Nat. Commun.* **8**, 15014 (2017).
63. M. Smutny *et al.*, Friction forces position the neural anlage. *Nat. Cell Biol.* **19**, 306–317 (2017).
64. L. G. Pimpale, T. C. Middelkoop, A. Mietke, S. W. Grill, Cell lineage-dependent chiral actomyosin flows drive cellular rearrangements in early Caenorhabditis elegans development. *Elife* **9**, 842922 (2020).
65. D. Pinheiro *et al.*, Transmission of cytokinesis forces via E-cadherin dilution and actomyosin flows. *Nature* **545**, 103–107 (2017).
66. A.C. Reymann *et al.*, Nucleation geometry governs ordered actin networks structures. *Nat. Mater.* **9**, 827–832 (2010).
67. M. P. Murrell, M. L. Gardel, F-actin buckling coordinates contractility and severing in a biomimetic actomyosin cortex. *Proc. Natl. Acad. Sci. U.S.A.* **109**, 20820–20825 (2012).
68. E. L. Suzuki *et al.*, Geometrical constraints greatly hinder formin mDia1 activity. *Nano Lett.* **20**, 22–32 (2020).
69. A. Azioune, M. Storch, M. Bornens, M. Théry, M. Piel, Simple and rapid process for single cell micropatterning. *Lab Chip* **9**, 1640–1642 (2009).
70. L. C. Kam, S. G. Boxer, Cell adhesion to protein-micropatterned-supported lipid bilayer membranes. *J. Biomed. Mater. Res.* **55**, 487–495 (2001).
71. Sonal *et al.*, Myosin-II activity generates a dynamic steady state with continuous actin turnover in a minimal actin cortex. *J. Cell Sci.* **132**, jcs219899 (2019).
72. C. G. Muresan *et al.*, F-actin architecture determines constraints on myosin thick filament motion. *Nat. Commun.* **13**, 7008 (2022).
73. R. Grover *et al.*, Transport efficiency of membrane-anchored kinesin-1 motors depends on motor density and diffusivity. *Proc. Natl. Acad. Sci. U.S.A.* **113**, E7185–E7193 (2016).
74. A. Sciortino, A. R. Bausch, Pattern formation and polarity sorting of driven actin filaments on lipid membranes. *Proc. Natl. Acad. Sci. U.S.A.* **118**, e2017047118 (2021).

75. H. Ennomani *et al.*, Architecture and connectivity govern actin network contractility. *Curr. Biol.* **26**, 616–626 (2016).
76. B. A. Smith *et al.*, Three-color single molecule imaging shows WASP detachment from Arp2/3 complex triggers actin filament branch formation. *Elife* **2**, e01008 (2013).
77. M. Soares e silva, B. Stuhrmann, T. Betz, G. H. Koenderink, Time-resolved microrheology of actively remodeling actomyosin networks. *New J. Phys.* **16**, 075010 (2014).
78. E. M. Kovacs, M. Goodwin, R. G. Ali, A. D. Paterson, A. S. Yap, Cadherin-directed actin assembly: E-cadherin physically associates with the Arp2/3 complex to direct actin assembly in nascent adhesive contacts. *Curr. Biol.* **12**, 379–382 (2002).
79. B. Serrels *et al.*, Focal adhesion kinase controls actin assembly via a FERM-mediated interaction with the Arp2/3 complex. *Nat. Cell Biol.* **9**, 1046–1056 (2007).
80. I. M. Herman, N. J. Crisona, T. D. Pollard, Relation between cell activity and the distribution of cytoplasmic actin and myosin. *J. Cell Biol.* **90**, 84–91 (1981).
81. M. Raab *et al.*, Crawling from soft to stiff matrix polarizes the cytoskeleton and phosphoregulates myosin-II heavy chain. *J. Cell Biol.* **199**, 669–683 (2012).
82. D. Riveline *et al.*, Focal contacts as mechanosensors: Externally applied local mechanical force induces growth of focal contacts by an mDia1-dependent and ROCK-independent mechanism. *J. Cell Biol.* **153**, 1175–1186 (2001).
83. G. Giannone *et al.*, Lamellipodial actin mechanically links myosin activity with adhesion-site formation. *Cell* **128**, 561–575 (2007).
84. S. J. Streichan, M. F. Lefebvre, N. Noll, E. F. Wieschaus, B. I. Shraiman, Global morphogenetic flow is accurately predicted by the spatial distribution of myosin motors. *Elife* **7**, e27454 (2018).
85. C. R. Cowan, A. A. Hyman, Acto-myosin reorganization and PAR polarity in C. elegans. *Development* **134**, 1035–1043 (2007).
86. S. K. Vogel, Z. Petrasek, F. Heinemann, P. Schwille, Myosin motors fragment and compact membrane-bound actin filaments. *Elife* **2**, e00116 (2013).
87. K. Carvalho *et al.*, Cell-sized liposomes reveal how actomyosin cortical tension drives shape change. *Proc. Natl. Acad. Sci. U.S.A.* **110**, 16456–16461 (2013).
88. J. A. Spudich, S. Watt, The regulation of rabbit skeletal muscle contraction. I. Biochemical studies of the interaction of the tropomyosin-troponin complex with actin and the proteolytic fragments of myosin. *J. Biol. Chem.* **246**, 4866–4871 (1971).
89. H. Isambert *et al.*, Flexibility of actin filaments derived from thermal fluctuations. *J. Biol. Chem.* **270**, 11437–11444 (1995).
90. C. Egile *et al.*, Activation of the Cdc42 Effector N-Wasp by the Shigella flexneri Icsa protein promotes actin nucleation by Arp2/3 complex and bacterial actin-based motility. *J. Cell Biol.* **146**, 1319–1332 (1999).
91. S. C. Almo, T. D. Pollard, M. Way, E. E. Lattman, Purification, characterization and crystallization of Acanthamoeba profilin expressed in Escherichia coli. *J. Mol. Biol.* **236**, 950–952 (1994).
92. J. P. Robblee, A. O. Olivares, E. M. De La Cruz, Mechanism of nucleotide binding to actomyosin VI. *J. Biol. Chem.* **279**, 38608–38617 (2004).
93. E. M. De La Cruz, E. M. Ostap, H. L. Sweeney, Kinetic mechanism and regulation of myosin VI. *J. Biol. Chem.* **276**, 32373–32381 (2001).
94. A. Colin *et al.*, Recycling of the actin monomer pool limits the lifetime of network turnover. *EMBO J.* **42**, e112717 (2023).
95. P. O. Strale *et al.*, Multiprotein printing by light-induced molecular adsorption. *Adv. Mater.* **28**, 2024–2029 (2016).
96. J. Schindelin *et al.*, Fiji: An open-source platform for biological-image analysis. *Nat. Methods* **9**, 676–682 (2012).